Bitesize bundles F-actin and influences actin remodeling in syncytial *Drosophila* embryo development

Authors: Anna R. Yeh[1], Gregory J. Hoeprich[2], Bruce L. Goode[2], Adam C. Martin[1]

[1]Department of Biology, Massachusetts Institute of Technology, Cambridge, MA, USA

[2]Department of Biology, Brandeis University, Waltham, MA, USA

Abstract

Actin networks undergo rearrangements that influence cell and tissue shape. Actin network assembly and organization is regulated in space and time by a host of actin binding proteins. The *Drosophila* Synaptotagmin-like protein, Bitesize (Btsz), is known to organize actin at epithelial cell apical junctions in a manner that depends on its interaction with the actin-binding protein, Moesin. Here, we showed that Btsz functions in actin reorganization at earlier, syncytial stages of *Drosophila* embryo development. Btsz was required for the formation of stable metaphase pseudo-cleavage furrows that prevented spindle collisions and nuclear fallout prior to cellularization. While previous studies focused on Btsz isoforms containing the Moesin Binding Domain (MBD), we found that isoforms lacking the MBD also function in actin remodeling. Consistent with this, we found that the C-terminal half of BtszB cooperatively binds to and bundles F-actin, suggesting a direct mechanism for Synaptotagmin-like proteins regulating actin organization during animal development.

Introduction

During animal development, actin networks are tightly regulated and undergo dynamic rearrangements to promote morphogenesis (Camuglia et al., 2021; Lecuit and Yap, 2015; Sokac et al., 2023). However, the range of mechanisms that control actin network assembly and organization during development is still not fully understood. There are various levels at which actin must be regulated, which we describe here as three major levels. First, the nucleation and assembly of monomeric G-actin (globular actin) into polymeric F-actin (filamentous actin) are tightly regulated in both time and space. Spontaneous nucleation of actin is inhibited by many factors *in vivo* (Plastino and Blanchoin, 2019). Therefore, actin nucleators and assemblers such as the formin, Diaphanous (Dia), as well as the Arp2/3 complex are essential in driving actin polymerization. Dia assembles actin structures composed of linear (unbranched) filaments, whereas Arp2/3 complex assembles branched actin filament networks. Next is the organization of filamentous actin into higher-order structures, or networks, which involves a plethora of actin binding and bundling/crosslinking proteins such as Fascin/Singed, Filamin/Cheerio and Fimbrin (Cant et al., 1994; Davidson et al., 2019; Krueger et al., 2019; Tilney et al., 2000). These networks are important for structure, transport, and transducing mechanical forces across the organism. Crosslinking actin filaments not only governs the network's architecture but also its rigidity and contractile properties (Koenderink and Paluch, 2018). Finally, the actin network must be connected to the cell membrane through actin-binding proteins in order to provide structure and help induce cell shape changes (Chugh and Paluch, 2018). The ERM (Ezrin Radixin Moesin) family of proteins plays an essential role in this process (Algrain et al., 1993;

47 Gould et al., 1989). When activated by phosphorylation through kinases, ERM proteins
48 undergo a conformational change to reveal an F-actin binding and membrane protein-
49 binding site such that they can tether F-actin to membrane (Gary and Bretscher, 1995;
50 Zaman et al., 2021). Therefore, each cell must coordinate actin nucleation, assembly
51 and disassembly, along with higher-order levels of control such as organizing actin
52 networks and connecting these networks to cell membrane.

53 The early *Drosophila* embryo provides an optimal system in which to study actin
54 regulation due to its dynamic actin network rearrangements. At the earliest stages of
55 development, the embryo is a syncytium consisting of one cell with multiple nuclei in a
56 shared cytoplasm. The syncytium undergoes multiple rounds of synchronous modified
57 cell divisions lacking cytokinesis and intervening gap phases, called nuclear divisions
58 (Figure 1A) (Foe et al., 2000). Nuclear cycles (NC) 1-9 occur in the yolk at the center of
59 the embryo, and nuclei migrate to the apical surface of the embryo for NC 10-13 (Foe
60 et al., 2000). Centrosomes then help direct the formation of F-actin structures called
61 'caps' (Stevenson et al., 2002; Stevenson et al., 2001), which are positioned above the
62 syncytial nuclei. During each nuclear cycle, F-actin assembly drives the growth of actin
63 caps that expand into one another (Figure 1A). Collisions between neighboring caps
64 lead to the formation of pseudo-cleavage furrows, structures made up of both actin and
65 membrane (Zhang et al., 2018) (Figure 1A). Pseudo-cleavage furrows act as a barrier
66 between dividing spindles and are essential for proper nuclear divisions. Perturbing
67 pseudo-cleavage furrows with drugs or depleting actin-related proteins often results in
68 spindle collisions (Afshar et al., 2000; Callaini et al., 1992; Spracklen et al., 2019;
69 Sullivan et al., 1993; Webb et al., 2009; Zallen et al., 2002).

70 In addition to actin assembly, membrane trafficking is essential for syncytial
71 blastoderm development. When membrane trafficking is perturbed by knocking down
72 components of the trafficking machinery, such as Nuf and Rab11, pseudo-cleavage
73 furrows are shorter and resemble those in embryos defective in actin assembly (Cao et
74 al., 2008; Holly et al., 2015; Riggs et al., 2003; Rikhy et al., 2015; Rothwell et al., 1998;
75 Sherlekar et al., 2020). Together, these findings indicate that actin network
76 reorganization is coupled with membrane remodeling to create pseudo-cleavage
77 furrows. However, there is still much to uncover about the roles that actin and/or
78 membrane remodelers play in morphogenesis.
79 Synaptotagmin-like proteins (Slps) are potential candidates for coupling actin and
80 membrane remodeling during syncytial blastoderm development. Slps are conserved
81 across vertebrates and are characterized by an N-terminal Slp homology domain (SHD)
82 and two C-terminal C2 domains (Figure 1B). The mammalian SHD interacts with the
83 GTPase Rab27, and the C2 domain consists of the C2A and C2B domains that bind
84 membrane, sometimes in a calcium-dependent manner (Fukuda, 2002; Galvez-
85 Santisteban et al., 2012). Specifically, the C2A domain binds with high affinity to
86 $PI(4,5)P_2$ or $PI(3,4,5)P_3$ and the C2B domain binds with high affinity to $PI(4,5)P_2$
87 (Galvez-Santisteban et al., 2012; Lyakhova and Knight, 2014). A family of proteins
88 related to Slps are Slac2s, Synaptotagmin-like proteins lacking C2 domains, which
89 contain the SHD at their N-terminus but lack the C-terminal C2 domains (Figure 1B).
90 Slac2 proteins function as adaptor proteins for cargo transport, interacting with Rab27A
91 via their SHD, as well as Myosin Va via their myosin-binding sites found in the middle of
92 Slac2 (Fukuda et al., 2002). Interestingly, the C-termini of Slac2-a and Slac2-c also bind

93 G- and F-actin (Fukuda et al., 2002). Both Slps and Slac2s are Rab27 effectors
94 important for vesicle secretion. For example, Slp4 is necessary for proper exocytosis
95 and granule docking in the pancreas (Mizuno et al., 2016). During *de novo* epithelial
96 formation, Slp2-a is required for targeting vesicles to the apical surface in a PIP2
97 dependent manner, and Slp4-a couples these vesicles to apical plasma membrane to
98 generate lumen (Galvez-Santisteban et al., 2012). Overall, there are six Slp genes and
99 three Slac2 genes in mammals. The reasons for such a diverse array of Slp and Slac
100 genes and whether less complex metazoans have functional equivalents to this diverse
101 gene family are unknown.
102 *Drosophila* encodes a single Slp gene, *Bitesize* (*Btsz*) that plays a role in actin
103 cytoskeleton organization (Pilot et al., 2006b) similar to mammalian Slp4/granuphilin.
104 However, it is unclear whether Btsz contains an SHD, or plays a direct role in
105 exocytosis. Pilot et al. showed that Btsz is essential for maintaining adherens junctions
106 and epithelial integrity. They discovered that certain Btsz isoforms interact with the
107 membrane-cortex crosslinker, Moesin (Moe), via a Moesin binding domain (MBD)
108 (Figure 1C). Their observations supported a model in which Btsz binds
109 phosphoinositides via its C2A and C2B domains, localizing it to adherens junctions at
110 the apical surface of the cell where it recruits Moesin to regulate actin organization and
111 stabilize E-cadherin (Figure 1D). During tracheal morphogenesis, Btsz recruits Moesin
112 to the luminal membrane to promote proper actin organization (Jayanandanan et al.,
113 2014). Therefore, previous work has established the importance of Btsz in regulating
114 the actin cytoskeleton through Moesin. However, alternative splicing generates nine
115 different Btsz isoforms and most of them lack the exon that encodes the MBD (Figure

116 1C). This raises the question of whether these other Btsz isoforms have distinct
117 functional roles in development, and how the functions of these isoforms may be related
118 to mammalian Slp and Slac2.

119 In this study, we discovered a role for Btsz in regulating actin organization during
120 syncytial stages of *Drosophila* embryo development, which in turn impacts spindle and
121 nuclear morphology. This function of Btsz is mediated in part by Btsz isoforms lacking
122 the Moesin-binding domain. We demonstrated this by making a CRISPR allele that
123 affects Btsz isoforms lacking the MBD as well as an isoform-specific
124 UAS>Btsz::mCherry tool to assess the localization of an individual isoform. Despite
125 lacking the MBD, we found that Btsz isoform B directly binds to F-actin and bundles F-
126 actin *in vitro*, suggesting a more direct role for Btsz in regulating actin architecture.

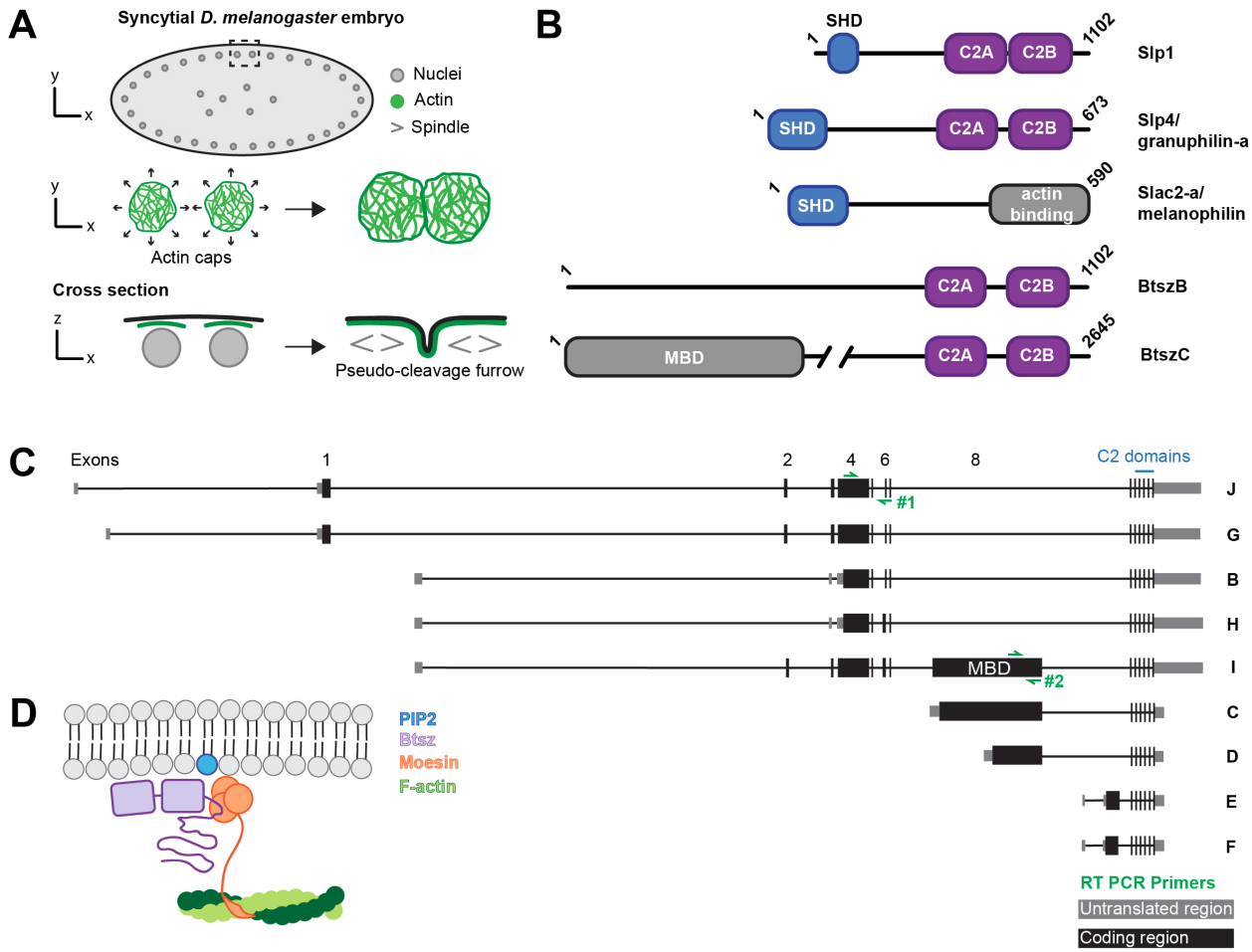

Figure 1. **Btsz is a Synaptotagmin-like protein (Slp) with multiple splice isoforms. (A)** Cartoon depiction of a syncytial embryo during a nuclear cycle. Top-down view of a syncytial embryo (top row). Zoomed in view of the actin caps in the dashed rectangular box where actin caps grow and collide with neighboring actin caps (middle row). Cross section of the zoomed in view where pseudo-cleavage furrows form from actin caps that have collided (bottom row). **(B)** Schematic of mammalian (mouse) Slp1, Slp4, Slac2-a, and fly Btsz isoform B and C proteins. **(C)** Schematic of the nine splice isoforms of the Btsz protein. Letters on the left-hand side denote the isoform name. Location of RT-PCR primer pairs #1 and #2 for exons 4-6 and exon 8, respectively, are shown with green arrows. **(D)** Model depicting Btsz's interaction with the plasma membrane and Moesin. Btsz and Moesin localized to apical membrane through interactions with PIP2. There, Btsz can bind the FERM3 domain of Moesin and Moesin binds F-actin.

Results

Btsz is required for actin remodeling during syncytial blastoderm development

To examine Btsz function in early development, we used an RNAi line to maternally deplete embryos of Btsz (Figure S1A). This shRNA targets a sequence in the 3' UTR shared by all isoforms. Past work on Btsz focused on isoforms containing the

144 Moesin-binding domain (MBD) and their roles during gastrulation in regulating actin
145 organization, epithelial integrity, and lumen formation (Jayanandanan et al., 2014;
146 Pilot et al., 2006b). Upregulation of Btsz isoforms containing the MBD at the mid-
147 blastula transition was noted in previous studies (Pilot et al., 2006a). We observed
148 that knock-down of all Btsz isoforms revealed striking defects in syncytial embryo
149 development as well as defects after epithelium formation, during gastrulation. We
150 found that 60% of Btsz-RNAi embryos displayed syncytial or cellularization defects
151 compared to 13% of control embryos (Figure S1B). Because defects prior to
152 gastrulation in Btsz-depleted embryos have not been described, and the syncytial
153 blastoderm is an excellent system in which to study actin remodeling, we further
154 investigated Btsz function in the syncytial blastoderm.

155 To determine Btsz function in syncytial stages of embryonic development, we
156 visualized actin in live embryos by driving mCherry::MoesinABD (mCh::Moe)
157 expression with the maternal Gal4 driver mat67 to observe actin cap and pseudo-
158 cleavage furrow structure and dynamics (Xie et al., 2021). We found that Btsz
159 depletion affected actin cap organization dynamics (Figure 2A; Video 1). We
160 measured cap size once the caps had finished expanding in control and Btsz-RNAi
161 embryos. Our results show that in Btsz-depleted embryos, the average cap area is
162 smaller compared to those of control embryos (Figure 2A-B). When comparing the
163 distribution of cap areas, there is a bimodal distribution of cap sizes and a greater
164 proportion of small actin caps (<80mm^2) in Btsz-shRNA embryos compared to the
165 control (Figure 2B-B’’).

166 Actin cap expansion and subsequent collisions between neighboring caps
167 drive pseudo-cleavage furrow formation and growth (Zhang et al., 2018) so we
168 hypothesized that pseudo-cleavage furrows would be affected in Btsz-RNAi
169 embryos. Interestingly, small actin caps in Btsz-depleted embryos still formed
170 pseudo-cleavage furrows between nuclei. Live imaging of actin in pseudo-cleavage
171 furrows did reveal that a higher frequency of furrows prematurely retract during
172 mitosis in Btsz-RNAi embryos (Figure 2C, D; Video 2). These unstable furrows
173 formed normally (Figure 2C, yellow arrows) but receded during metaphase, resulting
174 in furrows that are either very short or no longer visible (Figure 2C, red arrows).
175 However, pseudo-cleavage furrows that formed properly and did not retract in Btsz-
176 RNAi embryos reached their maximum length and were comparable in length to
177 wild-type furrows (Figure S2A, B).

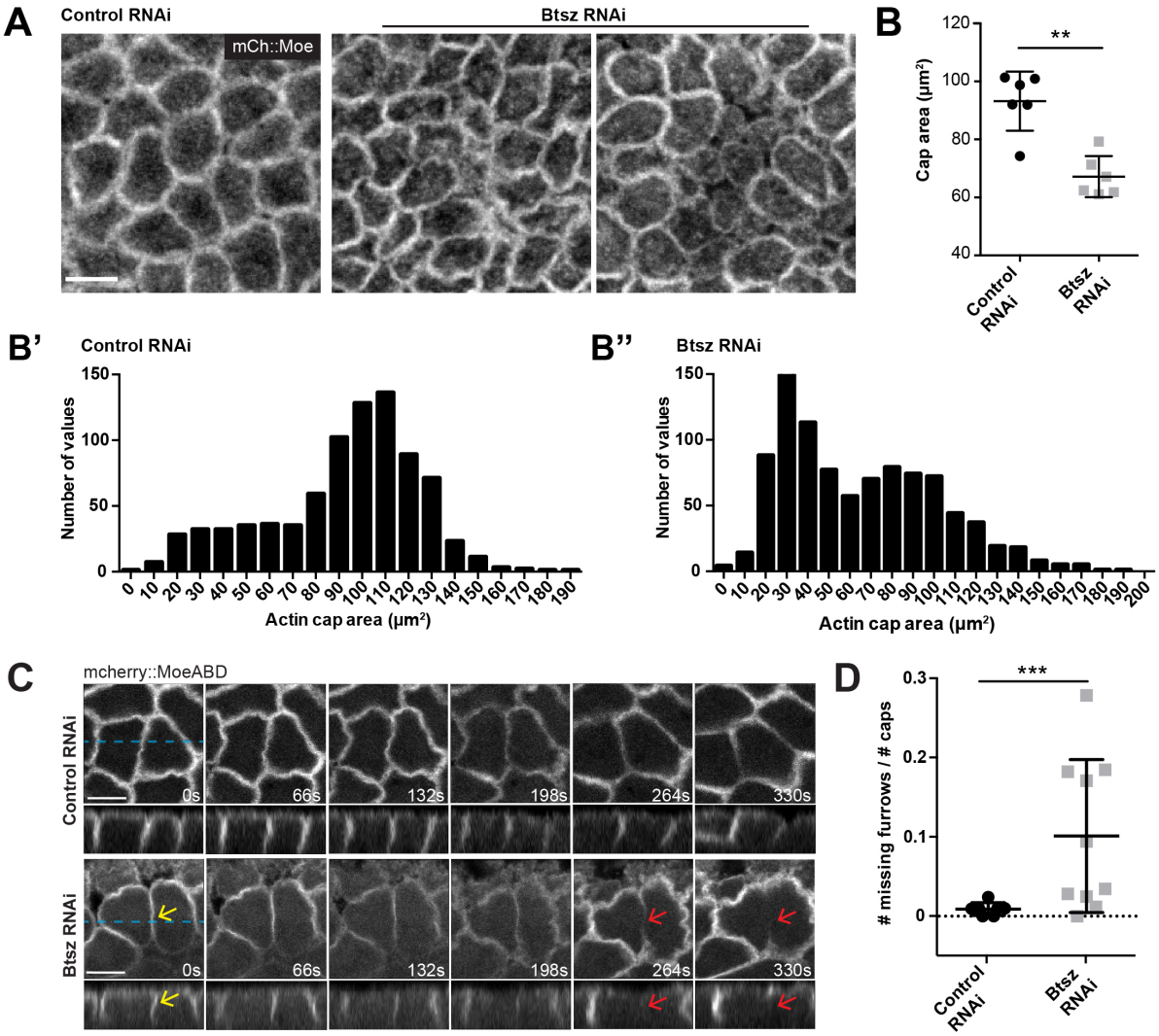

Figure 2. **Btsz is required for actin remodeling during syncytial blastoderm development. (A)** Maximum projection of a top-down view of control and Btsz RNAi nuclear cycle 12 actin caps. Actin was visualized live using the mCherry::MoesinABD marker. **(B)** In Btsz-depleted embryos, the average cap size is smaller compared to those in the control. Each data point is an average of all caps in the field of view per embryo. n = 6 embryos for both control RNAi and Btsz RNAi. p = 0.0043, Mann-Whitney U test. **(B', B'')** Histogram of raw data of actin cap area from Figure 2B. There is a peak of small actin caps (~30 µm^2) in Btsz RNAi embryos that is absent in the control embryos. **(C)** Time-lapse showing the formation of pseudo-cleavage furrows in control and Btsz-depleted embryos, with single slices (top panels) and orthogonal views (bottom panels). Actin was visualized live using the mCherry::MoesinABD marker. In Btsz RNAi embryo, a pseudo-cleavage furrow forms normally (yellow arrows), but breaks and recedes (red arrows) during metaphase while neighboring furrows are at their maximum length. **(D)** Number of missing furrows normalized over total number of actin caps. In Btsz-depleted embryos, pseudo-cleavage furrows prematurely recede during mitosis more often than in wild type embryos. Each point is the ratio of missing furrows to actin caps in a field of view (212 x 106 µm) per embryo. n = 7 embryos for control RNAi, n = 10 embryos for Btsz RNAi, p = 0.0007, Mann-Whitney U test. Scale bars are 10 µm.

197

198 **Btsz depletion leads to spindle collision and nuclear defects**

199 Because pseudo-cleavage furrows are essential for preventing spindle collisions
200 during each nuclear cycle, we assessed the integrity of the nuclear divisions in Btsz-
201 depleted embryos. Using the microtubule plus-end-tracking protein CLIP170 fused
202 with GFP to visualize spindles, we found that aberrant spindle morphology
203 accompanied *Btsz* knock-down (Figure 3A, C). In Btsz-depleted embryos, spindles
204 were often abnormally fused between neighboring nuclei (Figure 3A). This spindle
205 collision phenotype has been noted in various conditions where proteins that
206 regulate actin and/or membrane remodeling are disrupted (Dia, Arp2/3, Par1, APC2,
207 Abl, Nuf, Rab11, etc.) (Grevengoed et al., 2003; Jiang and Harris, 2019; McCartney
208 et al., 2001; Riggs et al., 2003; Rothwell et al., 1998; Webb et al., 2009; Zhang et al.,
209 2018).

210 Proper actin cytoskeleton regulation is important for centrosome migration to
211 opposite poles during nuclear division cycles (Cao et al., 2008). Centrosome
212 separation was abnormal in Btsz-depleted embryos (Figure 3B) with centrosomes
213 failing to migrate to 180° opposite each other prior to nuclear envelope breakdown
214 more often than in wild-type embryos (Figure 3B, C'). Both the distance between
215 centrosomes (Figure 3C'') and spindle length (Figure 3C''') were shorter in Btsz-
216 depleted embryos compared to wild-type embryos. These phenotypes were
217 reminiscent of those observed in other actin and APC2 mutants (Cao et al., 2008;
218 McCartney et al., 2001). Fixed imaging of both F-actin and nuclei during

219 cellularization revealed heterogeneity in compartment sizes and nuclear morphology
220 in Btsz RNAi embryos, indicative of improper nuclear divisions (Figure 3D).
221 Visualizing both F-actin and spindles confirmed that furrow breakages in the
222 Btsz RNAi background led to two sets of spindles in the same compartment (Figure
223 S2C). These spindle abnormalities preceded massive nuclear fallout from the cell
224 cortex during syncytial stages and cellularization, observed through live imaging the
225 nuclear marker Histone::GFP (Figure 3E, yellow arrows; Video 3). Quantification of
226 relative nuclear density shows that there are fewer nuclei in Btsz-depleted embryos
227 compared to the control (Figure 3F), likely a consequence of the pseudo-cleavage
228 furrow defects (Figure 2C). Overall, these results demonstrate a critical role for Btsz
229 in embryo development, well prior to its known role in epithelial integrity during
230 gastrulation.

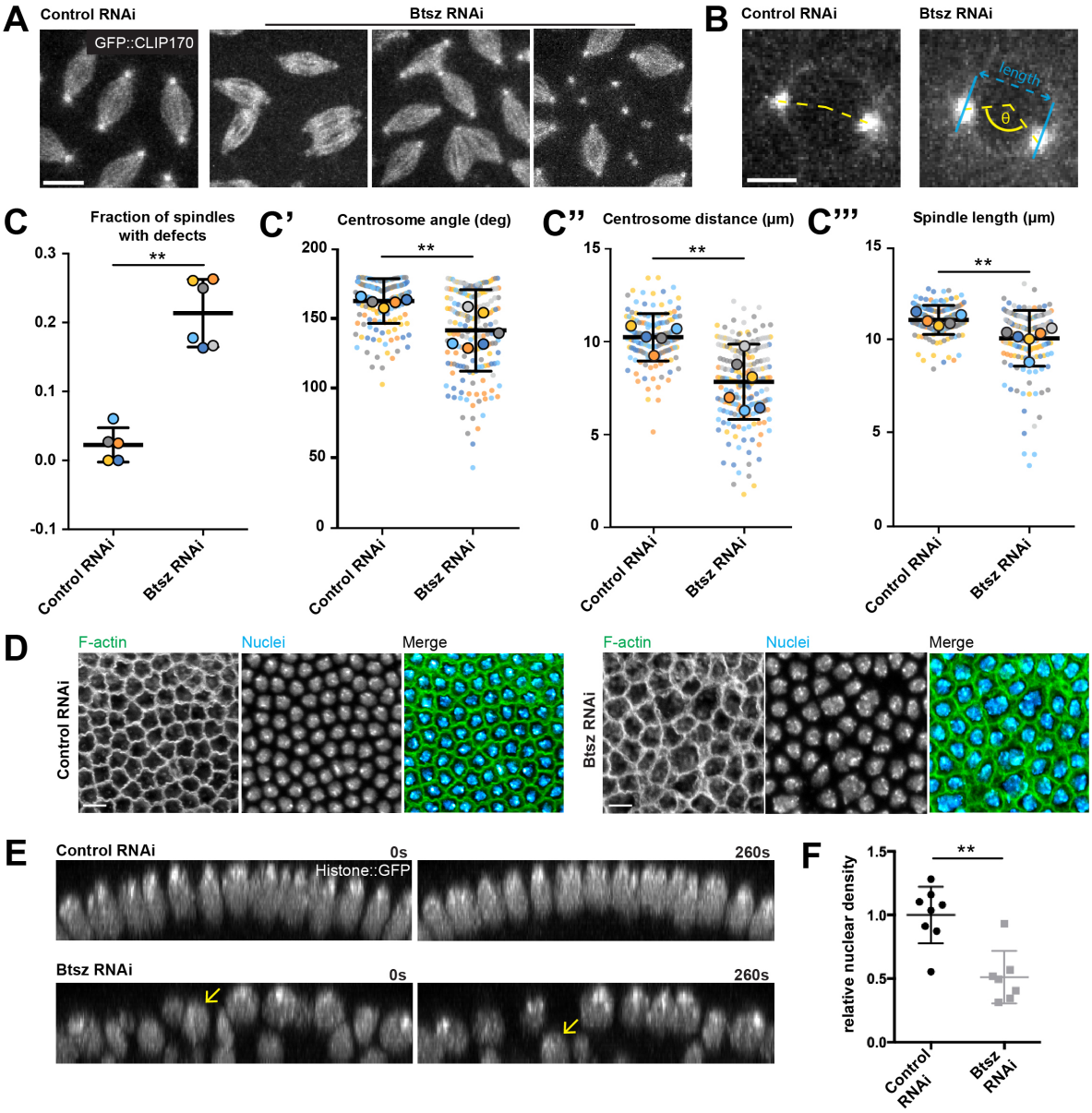

Figure 3. **Btsz-depletion leads to spindle collision and nuclear defects. (A, B)** Maximum projections of spindles and centrosomes visualized live using GFP::CLIP170 in control and Btsz-depleted embryos. Spindle collisions and aberrant centrosome morphology occur more frequently in Btsz-RNAi embryos. Scale bars are 10 µm for spindles, 5 µm for centrosomes. **(C)** Fraction of spindles that have collided in control and Btsz RNAi embryos. Each large, bold circle is the fraction of occurrences in an embryo **(C'-C''')** Quantification of shortest distance between a centrosome pair (cyan line), angle of a vertex drawn between a centrosome pair (yellow dashed line), and spindle length. Each large, bold circle is the average of one embryo and smaller circles of corresponding color are the centrosome pairs or individual spindles used in the analysis. n = 5 embryos for control RNAi, n = 6 embryos for Btsz RNAi. p = 0.0043 for fraction with defects, 0.0087 for centrosome distance and angle, 0.0043 for spindle length, Mann-Whitney U test. **(D)** Single slice of cellularizing control RNAi or Btsz RNAi embryos. F-actin was visualized using Phalloidin and nuclei was visualized using Hoechst in fixed samples. Both the actin cytoskeleton and nuclei are abnormal in Btsz RNAi embryos. **(E)** Orthogonal slice of nuclei visualized live using Histone::GFP at cellularization in control (top) or Btsz RNAi (bottom) embryos at 0s and 260s later. Yellow arrow indicates one nucleus at the surface of the Btsz RNAi embryo undergoing fallout.

(F) Nuclear fallout occurs more frequently in Btsz-depleted embryos compared to the control. Each point is the number of nuclei over area (nuclear density) in one embryo. p = 0.0043, Mann-Whitney U test.

Non-MBD and MBD containing Btsz isoforms are both important for development

Previous studies have focused on how Btsz regulates actin indirectly through Moesin and demonstrated that expression of MBD isoforms was induced at the maternal to zygotic transition (MZT) which occurs around 2-3 hours into development (Pilot et al., 2006a; Pilot et al., 2006b). However, only a minority of the Btsz isoforms contain the Moesin Binding Domain (MBD). We found that non-MBD isoforms were also developmentally upregulated at the MZT (Figure 4A). Thus, both “classes” of Btsz isoforms (those with or without MBD) could be important during development.

To test whether non-MBD Btsz isoforms specifically contribute to Btsz function, we used CRISPR/Cas9 to engineer a *btsz* mutant (*btsz exon 4*) with an early truncation present in the majority of non-MBD isoforms (Figure 4B). This truncation is also present in the BtszI isoform that contains both exon 4 and exon 8 (which contains the MBD) (Figure 1C). We compared these to germline clones of the $btsz^{K13\text{-}4}$ mutant, which has a deletion in the MBD-containing exon 8 (Figure 4B) (Serano and Rubin, 2003). Because Btsz-RNAi has an obvious nuclear density phenotype and live actin markers occasionally modified the furrow canal phenotypes (Spracklen et al., 2014), we analyzed the cytoskeleton network during cellularization using the non-muscle myosin II marker, Spaghetti squash::GFP (Sqh::GFP). We found that *btsz exon 4* embryos that are maternal and zygotic homozygous for the mutation exhibited noticeable nuclear fallout and abnormal cellularization compared to the wildtype. In $btsz^{K13\text{-}4}$ and *btsz exon 4* mutants, the myosin network constricted

273 over the space where nuclei had fallen out, resembling Btsz-RNAi embryos though
274 not as severe (Figure 4C, D). In addition, germline clones of the *btsz*$^{K13\text{-}4}$ mutant
275 affected nuclear density, with the myosin network constricting over the space where
276 nuclei had fallen out (Figure 4D, E). Taken together, our data suggest that Btsz
277 functions in the early embryo in a manner that is not entirely dependent on the MBD-
278 containing isoforms.

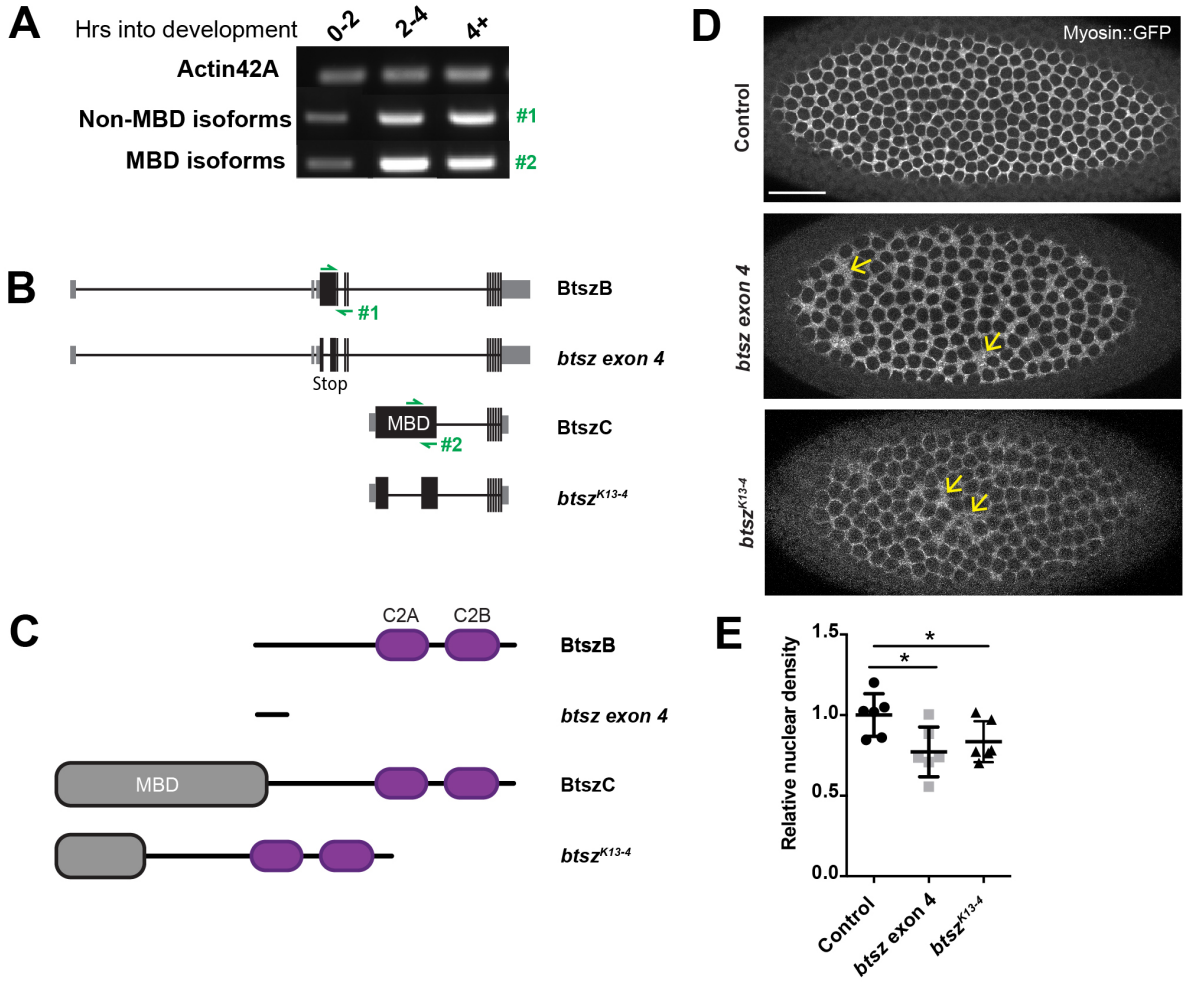

279

280 Figure 4. **Non-MBD containing Btsz isoforms are important for development**. **(A)** Gel of RT-PCR
281 products measuring isoform expression over developmental time. Both non-MBD isoforms and MBD
282 isoforms are upregulated during the maternal to zygotic transition (MZT). Primer pair #1 detected non-
283 MBD isoforms and primer pair #2 detected MBD-containing isoforms as indicated in green. **(B)**
284 Schematic of Btsz isoforms B and C, along with Btsz mutants *btsz exon 4 (*which was generated in this
285 study) and *btsz*$^{K13\text{-}4}$**.** *btsz exon 4* has an early truncation in exon 4, and *btsz*$^{K13\text{-}4}$ has a deletion in exon
286 8. **(C)** Schematic of the protein products of the Btsz isoforms shown in (B). **(D)** Maximum projection
287 images of cellularizing live embryos expressing Spaghetti squash::GFP (Sqh::GFP). Labeling

288 myosin allows for visualization of the cytoskeletal network to count nuclei. Yellow arrows indicate
289 gaps where nuclei have dropped out that have been filled in by the myosin network. Scale bar is
290 25 μm. **(E)** Relative nuclear density in *btsz exon 4* and *btsz*$^{K13-4}$ mutants, compared to controls. p
291 = 0.0260 for both comparisons, Mann-Whitney U test.
292
293 **BtszB binds and bundles F-actin**

294 Given the defects in actin-related processes exhibited by Btsz-RNAi and Btsz mutants,
295 we hypothesized that non-MBD Btsz may directly interact with actin. We examined
296 BtszB function *in vitro* because it is the shortest isoform that contains exons 4 through
297 7, which are shared by the majority of Btsz isoforms, and the C2 domains which are
298 shared by all Btsz isoforms. BtszB does not contain the MBD detailed in previous work
299 (Pilot et al., 2006b). Full-length BtszB was prone to degradation and the N-terminal
300 fragment of BtszB tended to pellet on its own, making F-actin cosedimentation assays
301 with these proteins difficult to interpret. However, a purified C-terminal fragment of
302 BtszB (BtszB-CT) demonstrated good expression and solubility. The BtszB-CT N-
303 terminus is within exon 6 and the fragment contains the C2A and C2B domains (Figure
304 5A). Notably, the BtszB-CT fragment is present in the majority of Btsz isoforms.
305 We performed high-speed pelleting assays to test whether Btsz-CT binds to actin
306 filaments and low-speed pelleting assays to test whether Btsz-CT bundles actin
307 filaments. In high-speed pelleting assays, a fixed concentration of BtszB-CT was mixed
308 with variable concentrations of F-actin, and then the amount of BtszB-CT bound to F-
309 actin was determined by analyzing the supernatant and pellet fractions on gels. With
310 increasing concentrations of F-actin, BtszB-CT shifted from the supernatant to the pellet
311 (Figure 5B). The data best fit a cooperative binding model with a binding affinity (K_d) of
312 0.45 μM and a Hill coefficient (h) of 2.9 (Figure 5C). In low-speed pelleting assays, F-
313 actin alone did not pellet significantly, but the addition of BtszB-CT shifted F-actin to the

314 pellet (Figure 5D and E), suggesting that BtszB-CT organizes F-actin into higher order
315 structures. These effects were confirmed independently through direct visualization in
316 TIRF microscopy assays, where BtszB-CT organized F-actin into bundles with
317 increased fluorescence and thickness (Figure 5F and G). Overall, these results show
318 that BtszB-CT binds directly and cooperatively to F-actin (K_d = 0.45 μM) and organizes
319 actin filaments into bundles, suggesting that all Btsz isoforms may bind and bundle F-
320 actin.

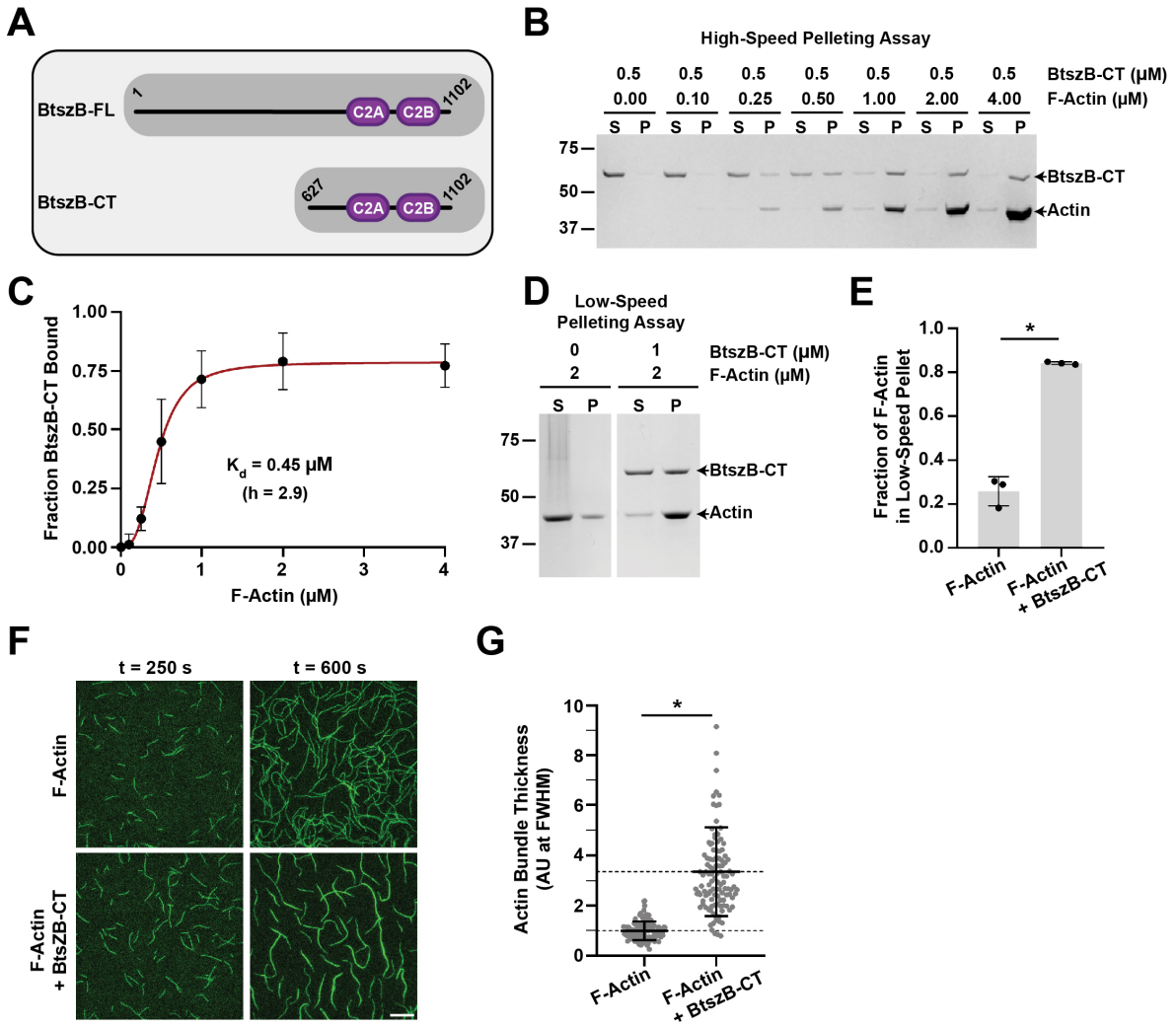

321

322 Figure 5. **The C-terminus of BtszB cooperatively binds and bundles actin filaments. (A)** Schematic
323 of full length BtszB (BtszB-FL) for reference and the C-terminal fragment (BtszB-CT) that was used in
324 the F-actin binding and bundling assays. **(B)** High-speed F-actin co-sedimentation assay varying the
325 F-actin concentration (0.1 - 4 μM) in the presence of 0.5 μM BtszB-CT. F-actin and BtszB-CT samples

were incubated together at room temperature for 30 min and then centrifuged (20 min at 25°C, 316k x g). **(C)** The fraction of BtszB-CT bound to actin filaments at increasing concentrations of F-actin was fit to a cooperative binding model with a K_d of 0.45 μM and a hill coefficient (h) of 2.9. Error bars are SD, n = 3. **(D)** Low-speed F-actin co-sedimentation assay using 2 μM F-actin with and without 1 μM BtszB-CT. F-actin and BtszB-CT were mixed together and incubated at room temperature for 30 min, then centrifuged (10 min at room temperature, 16k x g). **(E)** The fraction of F-actin pelleted with and without BtszB-CT. Error bars are SD, n = 3. p-value < 0.001, Student's t-test. **(F)** Representative time-lapse images from TIRF microscopy reactions containing 2 μM G-actin (10% Alexa 488-labeled) polymerized into filaments 10-20 μm in length, and then buffer or 1 μM BtszB-CT was flowed into the reaction chamber at 300 s and monitored for an additional 300 s. Scale bar is 20 μm. **(G)** Filament/bundle thickness was assessed by measuring the fluorescence intensity at FWHM (full width at half maximum) from line segments drawn perpendicular to the filament or bundle. Fluorescence intensity values were normalized to the mean intensity value of the control reaction (2 μM F-actin). Horizontal dashed lines are at y = 1, mean 2 μM F-actin control reaction, and y = 3.4, mean 2 μM F-actin + 1 μM BtszB-CT. ($n_{experiments}$ = 3, $n_{line\ segment}$ measurements for 2 μM F-actin = 41, 40, 42 and 1 μM BtszB-CT = 24, 35, 57. Error bars are SD, * is p-value < 0.001, Mann-Whitney U test).

Btsz localizes to apical junctions and pseudo-cleavage furrows

Next, we wanted to determine whether Btsz localizes to pseudo-cleavage furrows where actin binding and bundling are important for syncytial development. BtszF is one of the shortest Btsz isoforms (Figure 1C), containing only the C2 domains that are necessary for proper localization and one additional exon. We observed that BtszF localized to these furrows but did not completely co-localize with F-actin (Figure 6A). Given that past work indicates that the C2 domains are responsible for Btsz localization patterns (Pilot et al., 2006b), our data suggest that other Btsz isoforms localize similarly to BtszF in the syncytium.

To further explore the role of Btsz in actin binding and bundling *in vivo*, we examined actin organization in Btsz RNAi conditions. Btsz is upregulated during the MZT, similar to a subset of proteins that regulate F-actin levels in furrow canals, a distinct compartment that forms at the tip of cellularization furrows (Krueger et al., 2019; Schejter and Wieschaus, 1993; Sokac and Wieschaus, 2008; Zheng et al., 2013). Therefore, we wondered whether Btsz could be affecting F-actin at cellularization. We measured the ratio of actin intensity in the apical region of the

359 furrow to that in the furrow canals and saw no significant difference in Btsz-RNAi
360 embryos compared to control (Figure 6B, C).
361 To determine whether non-MBD isoforms localize to a compartment that is
362 distinct from furrow canals, we generated a fly line expressing BtszB N-terminally
363 tagged with mCherry. Fixed imaging revealed largely apical membrane localization
364 during cellularization and gastrulation (Figure 6D). This result aligns with previous
365 work that described the MBD-containing Btsz isoforms' localization and role in
366 regulating apical cell junctions (Pilot et al., 2006b). Unlike other actin cross-linkers
367 involved in cellularization, BtszB did not localize to furrow canals, suggesting that the
368 cellularization phenotypes we observed in Btsz mutants and Btsz RNAi (Figure 4D)
369 were the result of prior syncytial division defects. We propose that Btsz binds the
370 membrane through its C2 domains where Btsz organizes actin along the membrane
371 (Figure 6E).

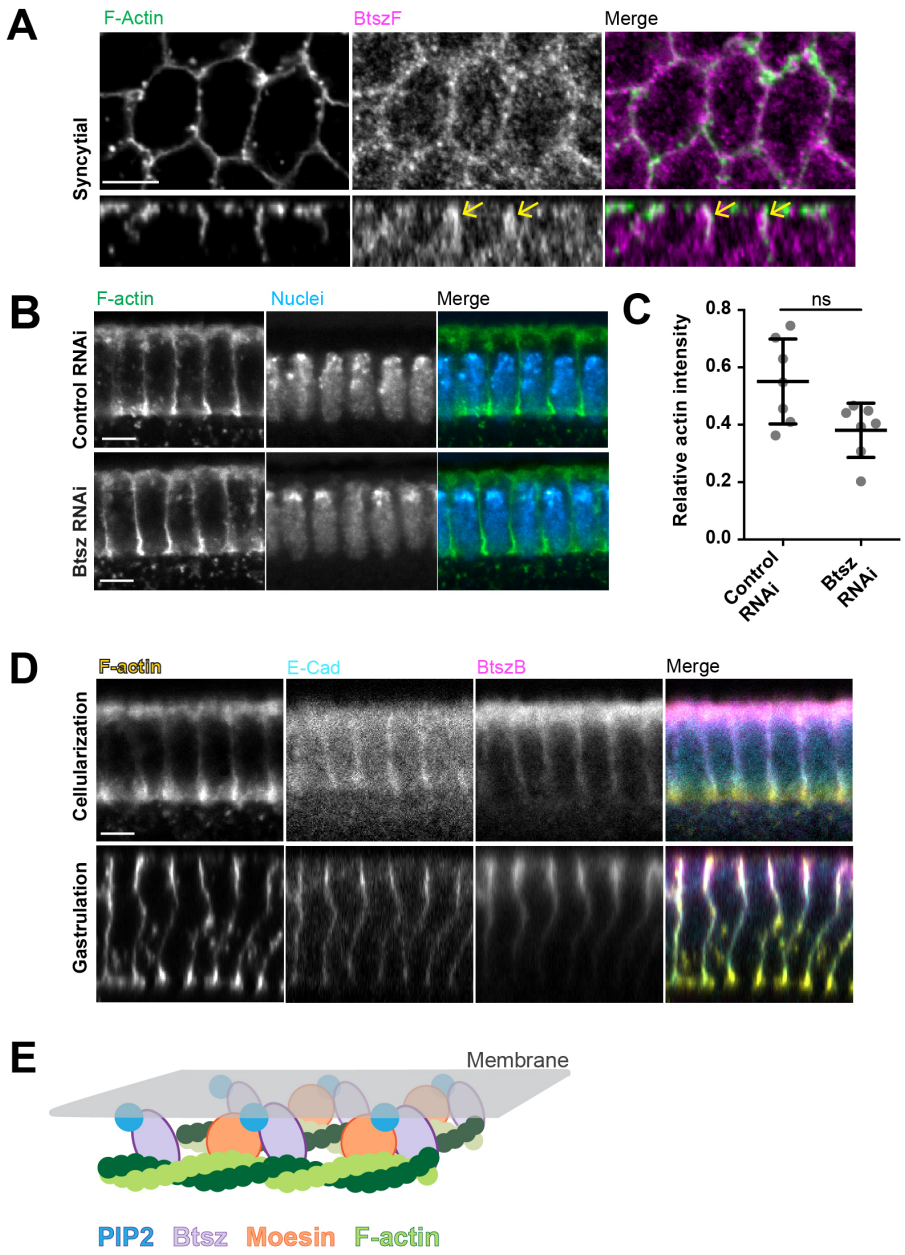

Figure 6. **Btsz localizes to pseudo-cleavage furrows and BtszB localizes to apical junctions and** **(A)** Maximum projection of a top-down view of the F-actin network and Btsz isoform F localization in the syncytium. BtszF localizes to pseudo-cleavage furrows (yellow arrows). Scale bars are 5 µm. **(B)** Cross section of fixed control RNAi or Btsz RNAi embryos during cellularization. F-actin was visualized using Phalloidin and nuclei was visualized using Hoechst. **(C)** There is no significant difference between the relative F-actin intensity (ratio of actin intensity in the apical region to that of the furrow canals) in the wildtype and Btsz-RNAi embryos. Mann-Whitney U test. **(D)** Cross sections of fixed control embryos, and embryos overexpressing mCherry::BtszB under the UASt promoter during cellularization (top) or gastrulation (bottom). F-actin (Phalloidin) in yellow, E-cadherin or junctions (α-Ecad) in cyan, and BtszB (α-RFP) in magenta. BtszB localizes apically during cellularization and gastrulation. **(E)** Schematic of how Btsz non-MBD and MBD isoforms may interact with Moesin and/or F-actin at the membrane to bundle and organize the cytoskeleton.

386 **Discussion**

387 Our data show that the Synaptotagmin-like protein Btsz can directly regulate
388 actin networks in addition to functioning through Moesin. We found that depletion of
389 either MBD or non-MBD isoforms resulted in syncytial embryo defects similar to
390 those caused by other mutants and perturbations that affect actin organization. In
391 addition, we showed that a Btsz C-terminal fragment can cooperatively bind to F-
392 actin and promote F-actin bundling. This supports a model in which Btsz binds the
393 membrane through its C2 domains and promotes actin bundling along the
394 membrane.

395 Actin network organization must be tightly regulated for proper syncytial
396 blastoderm development. This precise regulation is orchestrated by a large group of
397 actin and membrane remodeling proteins to ensure proper nuclear divisions. Our
398 results reveal a novel role for Btsz in organizing actin in the syncytial *Drosophila*
399 embryo. In Btsz-RNAi embryos, actin caps were smaller and pseudo-cleavage
400 furrows were often defective, leading to spindle collisions and nuclear fallout which
401 resembled phenotypes from knocking down other known actin regulators (Afshar et
402 al., 2000; Stevenson et al., 2002; Zallen et al., 2002). In *btsz exon 4* and *btsz*$^{K13\text{-}4}$
403 mutants, we saw evidence of nuclear fallout, similar to, but less severe than the
404 Btsz-RNAi defects, suggesting that both sets of isoforms contribute to Btsz function.
405 Taken together, the data suggest that Btsz can promote higher-order F-actin
406 network structure by bundling F-actin, and by connecting these networks to
407 membrane.

408

409 **Btsz regulates actin organization at multiple stages of early *Drosophila***
410 **embryo development**

411 Our *in vitro* data indicate that the BtszB isoform binds and bundles F-actin,
412 shedding light on how Btsz may regulate actin *in vivo* in a complementary manner to
413 previously published work (Jayanandanan et al., 2014; Pilot et al., 2006b; Zhang et
414 al., 2018). While some Btsz isoforms bind Moesin, our data predict that most or all
415 isoforms bind and bundle F-actin. In the related Slac2 protein, Melanophilin, the
416 actin binding domain (ABD) is also at the C-terminus (Kuroda et al., 2003). Btsz is
417 therefore another Synaptotagmin-related protein that can directly interact with actin.

418 In the syncytium, Btsz could promote actin filament bundles generated by the
419 formin Diaphanous (Jiang and Harris, 2019). BtszF contains the C2 domains and
420 localizes to syncytial pseudo-cleavage furrows. Because all Btsz isoforms contain
421 the C2 domains responsible for membrane localization, it is possible that all isoforms
422 localize the same way. Btsz bundling may stabilize actin at the pseudo-cleavage
423 furrows and prevent their recession, as furrows in Btsz-depleted embryos often
424 break and retract to the surface. Because each round of nuclear division occurs
425 rapidly (within ~8-10 minutes), pseudo-cleavage furrow growth requires dynamic
426 membrane and actin remodeling. During oogenesis, the *Drosophila* Fascin homolog,
427 Singed, is required for actin bundling when rapid actin polymerization takes place to
428 provide structural integrity for these bundles (Cant et al., 1994). Btsz may function in
429 a similar way, stabilizing F-actin bundles against disassembly during a time of rapid
430 actin remodeling.

431 Actin bundles are also a key component of adherens junctions (AJs), which
432 are critical for cell-cell adhesion. The dynamic coupling of the F-actin network to
433 adherens junctions is necessary for propagating forces across cells (Gorfinkiel and
434 Arias, 2007; Jodoin, 2015; Maître et al., 2012; Martin et al., 2010; Roh-Johnson et
435 al., 2012). E-cadherin (E-cad) is an important component of AJs, and its localization
436 is stabilized by F-actin. When Btsz is disrupted, so is actin organization which in turn
437 destabilizes E-cad, leading to defects in tissue integrity (Pilot et al., 2006b). As our
438 data show that BtszB is present at apical junctions (Figure 6D), we hypothesize that
439 Btsz binds and bundles F-actin to organize actin at these junctions (Figure 6E).

440 **Multiple Btsz isoforms exhibit upregulated gene expression at the maternal-**
441 **zygotic transition**

442 Precise gene expression of actin regulators is essential for proper
443 morphogenesis to ensure that actin networks are assembled and organized at the
444 correct time. The MZT is a conserved process where the developing embryo transitions
445 from being transcriptionally quiet to active (Lee et al., 2014). The expression of many
446 actin remodeling proteins necessary for cellularization, such as Bottleneck, Nullo, Slam,
447 Dunk, and Serendipity-α (Sry-α), are developmentally upregulated at the MZT (He et al.,
448 2016; Krueger et al., 2019; Lecuit et al., 2002; Postner and Wieschaus, 1994; Schejter
449 and Wieschaus, 1993; Simpson and Wieschaus, 1990; Sokac and Wieschaus, 2008;
450 Wenzl et al., 2010; Zheng et al., 2013). If the MZT is disrupted in *Drosophila*,
451 cellularization does not proceed. Our work reveals that Btsz is one of this group of
452 developmentally expressed F-actin binding/bundling proteins. However, Btsz is present
453 uniquely in an apical-lateral compartment distinct from the other actin-remodeling

454 proteins mentioned above, which each localize to furrow canals. In a *nullo* or *sry-α*
455 mutant background, F-actin levels are reduced in these furrow canals. While Btsz does
456 not appear to affect F-actin levels at the apical domain or in furrow canals (Figure 6B,
457 C), it is possible that Btsz localizes apically during cellularization when adherens
458 junctions form - in preparation for their role in maintaining junctions during gastrulation.
459 Alternatively, BtszB may play an undescribed role in the apical or lateral domains of
460 cellularization furrows.

461 **Possible functions for Btsz in membrane trafficking**

462 An important question that remains unanswered is whether Btsz plays a role in
463 *Drosophila* regulating membrane trafficking like mammalian Slps. Our work here
464 focused primarily on furthering our understanding of Btsz's role in actin organization.
465 For instance, Nuclear fallout (Nuf) is required for actin and membrane remodeling
466 during the syncytial divisions through its role in regulating trafficking (Riggs et al.,
467 2003). In *nuf* mutants, pseudo-cleavage furrows are defective leading to spindle
468 collisions and nuclear fallout (Rothwell et al., 1998). Considering the close coupling
469 between actin and membrane remodeling, as well as the spindle collisions and
470 nuclear fallout observed upon Btsz depletion, we cannot rule out that the phenotypes
471 we observe in Btsz-RNAi or *btsz* mutant embryos are in part due to defects in
472 vesicle trafficking.

473 **Materials and Methods**

474 **Fly stocks and genetics**

475 Fly stocks and crosses used in this study are listed in Supplementary File 1. For
476 crosses involving maternal gene depletion and overexpression, flies expressing

477 maternal Gal4 drivers were crossed to UAS-driven constructs and maintained at 25°C.
478 Nonbalancer F1 females were crossed to nonbalancer F1 males, and F2 embryos were
479 used for imaging.

480 For the *btsz exon 4* mutant, a deletion was generated at the endogenous Btsz
481 locus using CRISPR-Cas9 as previously described (Gratz et al., 2015). Two 15 base
482 pair (bp) gRNAs targeting sites in Btsz exon 4, roughly 500 bps apart, were identified
483 using flyrnai.org/crispr and cloned into the pCFD5 plasmid. This vector was constructed
484 and packaged by VectorBuilder and the vector ID is VB200707-1018qzm, which can be
485 used to retrieve further information about the vector on vectorbuilder.com. The plasmid
486 was injected into nanos-Cas9-expressing embryos by BestGene Inc (Chino Hills,
487 California). Surviving adults were crossed to Dr/TM3 flies and the deletion was
488 screened for using PCR. Flies with successfully a generated deletion were sequenced
489 for further analysis. For crosses involving *btsz exon 4*, crosses were set up using two
490 *btsz exon 4* lines of independent CRISPR alleles.

491 For crosses involving $btsz^{K13\text{-}4}$, the FLP-DFS technique was used to generate
492 mutant germline clones (Chou and Perrimon, 1992). We used *btszK13-4* alone and
493 sqh::GFP; $btsz^{K13\text{-}4}$ mutant stocks. Briefly, hsFLP;; Dr/TM3, Sb females were crossed to
494 FRT82B ovoD1/TM3, Sb males. hsFLP/Y;; FRT 82B ovoD1/Dr males were crossed to
495 $btsz^{K13\text{-}4}$ FRT/TM3, Sb or sqh::GFP; $btsz^{K13\text{-}4}$ FRT/TM3, Sb females. Larvae from this
496 cross were heat shocked for 2 hrs at 37°C for 3-4 days. hsFLP; + or sqh::GFP; $btsz^{K13\text{-}4}$
497 FRT/*ovoD* FRT females were crossed to OregonR males to collect embryos resulting
498 from the $btsz^{K13\text{-}4}$ germline clones.

499 The pUASt-mCherry::BtszB fly line was constructed using the coding sequence
500 of BtszB (generous gift from Thomas Lecuit, Collège de France). The vector used to
501 overexpress mCherry::Btsz in our study was constructed and packaged by
502 VectorBuilder (Chicago, Illinois). The vector ID is VB211103-1199vfw. This vector was
503 injected into attP40 flies and surviving adults were crossed to Sp/CyO flies. Presence of
504 the vector was screened for by presence of red eye color and confirmed with
505 subsequent PCR and sequencing.

506 **Live and fixed imaging**

507 Crosses were maintained at 25°C unless otherwise stated. Embryos were collected
508 from apple-juice agar plates and embryos were staged using Halocarbon 27 oil.
509 Embryos were then dechorionated in 50% bleach (Chlorox) for 2 minutes and rinsed
510 twice with water.

511 For live imaging, embryos were mounted on a slide with embryo glue (Scotch
512 tape dissolved in heptane). No. 1.5 coverslips were placed on the slide on either side of
513 the mounted embryos and a No.1 coverslip was used to cover the embryos and create
514 a chamber. This chamber was filled using Halocarbon 27 oil.

515 For fixed imaging involving Phalloidin staining, embryos were fixed using 4%
516 paraformaldehyde (Electron Microscopy Sciences) in 0.1M phosphate buffer at pH 7.4
517 with 50% heptane (Alfa Aesar) and manually devitellinated. Embryos were washed in
518 0.01% Triton X-100 in PBS (PBS-T), incubated in primary antibodies followed by
519 secondary antibodies (Supplementary File 1), and mounted onto a glass slide using
520 AquaPolymount (Polysciences).

521 Live and fixed images were taken using a Zeiss LSM 710 point scanning
522 confocal microscope with a 40x/1.2 C-Apochromat water objective lens or 63x/1.4 Plan-
523 Apochromat oil objective lens, an argon-ion, 405 nm diode, 594 nm HeNe, 633 HeNe
524 laser, and Zen software. Pinhole settings ranged from 1 to 2.5 Airy units. For two-color
525 live imaging, band-pass filters were set at ~410-513 nm for Hoechst, ~490–565 nm for
526 GFP, and ~590–690 nm for mCherry (mCh). For three-color imaging, band-pass filters
527 were set at ~480–560 nm for Alexa Fluor 488, ~580–635 nm for Alexa Fluor 568, and
528 ~660–750 nm for Alexa Fluor 647.

529 **Image processing and analysis**

530 Figure images were processed in FIJI or Matlab R2019b. For actin cap area and
531 nuclear fallout quantifications, images were run through a segmentation analysis
532 (detailed below) in Matlab. For all figures, brightness and contrast were adjusted
533 linearly. For Figures 2, 3, and 5, images were processed in FIJI with a Gaussian blur of
534 0.5. For Figure 6, images were processed in FIJI with a Gaussian blur of 0.5 and using
535 Subtract Background with a rolling ball radius of 50.0 pixels.

536 **Actin cap and cellularization furrow quantifications**

537 *Actin cap area and nuclear fallout*

538 Embryos expressing mCherry::Moe were used to visualize actin caps. To stage-match
539 embryos, we scored the size and number of actin caps. We measured actin cap area
540 during NC12 past the expansion phase of cap growth to minimize gaps in the actin
541 network. This was roughly 4 minutes before pseudo-cleavage furrows reach their
542 maximum depth during NC12. A maximum intensity projection (MIP) at this time point
543 was then used in a segmentation pipeline in MATLAB detailed below and manual

544 corrections were made in FIJI. To count nuclei, MIPs of embryos expressing Sqh::GFP
545 were segmented using the same Matlab procedure and FIJI was used to measure
546 embryo area in the given field of view and to count nuclei.

547 1. The intensity of each pixel was scaled up by a factor of 1.25.
548 2. Ridge-like structures in the image were enhanced with FrangiFilter2D
549 using the default parameters (Dirk-Jan Kroon (2022). Hessian based Frangi
550 Vesselness filter (https://www.mathworks.com/matlabcentral/fileexchange/24409-
551 hessian-based-frangi-vesselness-filter), MATLAB Central File Exchange); based
552 on (Frangi et al., 1998).
553 3. The resulting image was blurred via a Gaussian blur of sigma 4-10
554 depending on the image using Matlab's imgaussfilt() function.
555 4. Seeds for a watershed segmentation were automatically determined using
556 the imregionalmin() function on the blurred, background-subtracted image.
557 5. The ridge-enhanced image from step 2 was blurred with a median filter of
558 size 11 pixels, then the seeds were imposed as local minima on this image.
559 6. The watershed() function was used on this image to generate lines
560 corresponding to the boundaries between actin caps.

561 *Furrow actin intensity*

562 Cellularizing embryos were fixed and imaged to calculate the ratio of actin intensity in
563 the apical to basal regions in the furrows. FIJI was used to measure intensity. A ratio of
564 intensity was taken of the most apical and basal 2 μm of the furrows. Intensities were
565 normalized by rescaling values between 0 and 1 using $(I-I_{min})/(I_{max}-I_{min})$.

566 **Molecular biology**

567 For RNA extraction, thirty embryos were collected for each stage analyzed and ground
568 up in TRIzol reagent (Life Technologies, Inc.) using a motorized pestle mixer. mRNA
569 was extracted using TRIzol and chloroform. The aqueous phase was transferred into a
570 fresh tube and extraction continued using the Monarch RNA Cleanup Kit (NEB). The
571 extracted mRNA was treated with TURBO DNA-*free*™ (Invitrogen) and cDNA was
572 produced using Invitrogen SuperScript™ III First-Strand Synthesis System. Subsequent
573 PCR reactions were run with primers listed in (Supplementary File 1).

574 **Purification of BtszB**

575 Vectors of full-length BtszB and BtszB fragments were generated for protein expression
576 and purification (ABclonal Science Inc.). Full-length Btsz isoform B was insoluble in
577 bacteria and so we used the baculovirus system to express Btsz-B in Sf9 cells and
578 purified protein from those (ABclonal Science Inc).

579 **Purification and Labeling of Actin**

580 Rabbit skeletal muscle actin was purified from acetone powder (Spudich and Watt,
581 1971) generated from frozen ground hind leg muscle tissue of young rabbits (PelFreez).
582 Lyophilized acetone powder stored at -80°C was mechanically sheared in a coffee
583 grinder, resuspended in G-buffer (5 mM Tris-HCl [pH 7.5], 0.5 mM Dithiothreitol [DTT],
584 0.2 mM ATP, 0.1 mM $CaCl_2$), and then cleared by centrifugation for 20 min at 50,000 ×
585 g. The supernatant was filtered through Grade 1 Whatman paper, then the actin was
586 polymerized by the addition of 2 mM $MgCl_2$ and 50 mM NaCl and incubated overnight at
587 4°C. The final NaCl concentration was adjusted to 0.6 M to strip residual actin-binding
588 proteins, incubated at 4°C for 1 h, and then the F-actin was pelleted by centrifugation for
589 150 min at 361,000 × g. The pellet was solubilized by dounce homogenization and

590 dialyzed against 1 L of G-buffer at 4°C (three consecutive times at 12–18 h intervals).
591 Monomeric actin was then precleared at 435,000 × g and loaded onto a S200 (16/60)
592 gel-filtration column (GE Healthcare) equilibrated in G-Buffer. Peak fractions containing
593 actin were stored at 4°C.
594 To fluorescently label actin, G-actin was polymerized by dialyzing overnight against
595 modified F-buffer (20 mM PIPES [pH 6.9], 0.2 mM $CaCl_2$, 0.2mM ATP, 100 mM KCl)
596 (Shekhar, 2017). F-actin was incubated for 2 h at room temperature with Alexa 488
597 NHS ester dye (Life Technologies) at a final molar concentration 5 times in excess of
598 actin concentration. F-actin was then pelleted by centrifugation at 450,000 × g for 40
599 min at 4°C. The pellet was homogenized with a dounce and dialyzed overnight at 4°C
600 against 1 L of G-buffer (three consecutive times at 12–18 h intervals). Next, the solution
601 was centrifuged at 450,000 × g for 40 min at 4°C. The supernatant was collected and
602 loaded onto a S200 (16/60) gel-filtration column (GE Healthcare) equilibrated in G-
603 Buffer. Peak fractions containing labeled G-actin were pooled and the concentration and
604 labeling efficiency was determined by measuring the absorbance at 290 nm and 494
605 nm. Molar extinction coefficients used were as follows: ε_{290} actin = 26,600 M^{-1} cm^{-1} and
606 ε_{494} Alexa 488 = 71,000 M^{-1} cm^{-1}. The labeled G-actin was stored in G-Buffer + 50%
607 glycerol at -20°C and then dialyzed back into G-Buffer (no glycerol) for experiments.
608 **High-Speed and Low-Speed Pelleting (Co-Sedimentation) Assays**
609 F-actin was prepared by polymerizing 20 μM of G-actin with initiation mix (final
610 concentration: 2 mM $MgCl_2$, 0.5 mM ATP, 50 mM KCl) overnight at room temperature.
611 For high-speed pelleting assays, different concentrations of F-actin (0, 0.1, 0.25, 0.5, 1,
612 2, 4 μM) were incubated with 0.5 μM BtszB-CT for 30 min at room temperature.

613 Reactions were then centrifuged at 316,000 × g for 20 min at 25°C using a tabletop
614 Optima TLX Ultracentrifuge (Beckman Coulter). Supernatant and pellet fractions were
615 analyzed on Coomassie stained gels, and quantified by scanning densitometry using a
616 ChemiDoc Imaging System (BioRad). In calculating the fraction of BtszB-CT bound to
617 F-actin in each reaction, the BtszB-CT that pelleted nonspecifically (without F-actin) was
618 subtracted. Fraction of BtszB-CT bound at different concentrations of F-actin was
619 plotted, and fit to a Hill Equation using Prism (GraphPad). For low-speed pelleting
620 assays, 2 μM of F-actin was incubated with or without 1 μM BtszB-CT for 30 min at
621 room temperature. Reactions were then centrifuged at 16,000 × g for 10 min at room
622 temperature using a tabletop centrifuge (Eppendorf). Supernatant and pellet fractions
623 were analyzed on Coomassie stained gels and quantified as above. Fraction of F-actin
624 pelleted +/- BtszB-CT was plotted and compared statistically using a Mann-Whitney U
625 test from Prism (GraphPad).

626 **F-Actin Bundling TIRF Microscopy Assays and Image Analysis**

627 Glass coverslips (60 × 24 mm; Thermo Fisher Scientific) were first cleaned by
628 sonication in 1% Hellmanex™ III (Sigma-Aldrich) glass cleaner for 60 min at room
629 temperature, followed by successive sonications in 100% ethanol for 60 min and 1 M
630 KOH for 20 min. Coverslips were then washed extensively with H_2O and dried in an N_2
631 stream. The cleaned coverslips were coated with 2 mg/ml methoxy-polyethylene glycol
632 (PEG)-silane MW 2000 and 2 μg/ml biotin-PEG-silane MW 3400 (Laysan Bio, Arab, AL)
633 in 80% ethanol, pH 2.0, and incubated overnight at 70°C. Flow cells were assembled by
634 rinsing PEG-coated coverslips with water, drying with N_2, and adhering to μ-Slide VI0.1
635 (0.1 × 17 × 1 mm) flow chambers (Ibidi, Fitchburg, WI) with double-sided tape (2.5 cm ×

636 2 mm × 120 μm) and 5-min epoxy resin (Devcon, Danvers, MA). Before each reaction,
637 the flow cell was incubated for 1 min with 1% bovine serum albumin (BSA) in HEKG5
638 buffer (20 mM HEPES, pH 7.4, 1 mM EDTA, 50 mM KCl, and 5% glycerol), and then
639 equilibrated with TIRF buffer (10 mM imidazole, pH 7.4, 50 mM KCl, 1 mM $MgCl_2$, 1 mM
640 ethylene glycol-bis(β-aminoethyl ether)-N,N,N′,N′-tetraacetic acid (EGTA), 0.2 mM ATP,
641 10 mM DTT, 15 mM glucose, 20 μg/ml catalase, 100 μg/ml glucose oxidase) plus 0.5%
642 methylcellulose (4000 cP). Finally, 2 μM G-actin (10% Alexa 488–labeled on Cys 374)
643 polymerized to 10 - 20 μm, washed with TIRF buffer and then 1 μM BtszB-CT was
644 flowed into the reaction chamber 300 s after initiation of actin assembly. Upon flowing
645 wash TIRF buffer and BtszB-CT into the TIRF chamber, filament often would move
646 around but did not get flushed out because of the crowding agent (methylcellulose) in
647 the buffer.
648 Single-wavelength time-lapse TIRF imaging was performed on a Nikon-Ti2000 inverted
649 microscope equipped with a 150-mW argon laser (Melles Griot), a 60 × TIRF objective
650 with a numerical aperture of 1.49 (Nikon Instruments), and an electron-multiplying
651 charge coupled device (EMCCD) camera (Andor Ixon, Belfast, Ireland). One pixel was
652 equivalent to 143 × 143 nm. Focus was maintained by the Perfect Focus system (Nikon
653 Instruments). TIRF microscopy images were acquired every 5 s and exposed for 100
654 ms for at least 10 min using imaging software Elements (Nikon Instruments, New York,
655 NY).
656 Images were analyzed in FIJI version 2.0.0-rc-68/1.52e (National Institutes of Health,
657 Bethesda, MD). Background subtraction was conducted using the rolling ball
658 background subtraction algorithm (ball radius, 5 pixels). To measure actin filament

659 bundling, the line segment tool was used to draw a line perpendicular to actin
660 filaments/bundles in the FOV. The intensity profile of the line segment was fit to a 2-
661 dimensional Gaussian curve in FIJI. The intensity at full-width half-max (FWHM) for
662 each line trace was recorded at 300 s into the reactions (where BtszB-CT was flowed in
663 at time 0). All individual intensity measurements were normalized to the average actin
664 filament/bundle intensity from the control reaction (2 μM F-actin). A Mann-Whitney U
665 statistical test was performed to determine bundling activity between the control reaction
666 (2 μM F-actin) and the 1 μM BtsB-CT reaction.

667 **Statistical analysis**

668 All statistical analyses were carried out using GraphPad Prism or MATLAB.

669 **Acknowledgments**

670 We thank members of the Martin lab for helpful discussions and comments on the
671 manuscript. We thank Jonathan Jackson for writing the segmentation pipeline code. We
672 thank J. Solitro, Z. Li, and J. Eskin for their assistance with experiments. We are grateful
673 to Goode lab members for assistance with actin purification and labeling. Finally, we
674 thank the Bloomington Stock Center and the TRiP at Harvard Medical School (National
675 Institutes of Health/National Institute of General Medical Sciences R01-GM084947) for
676 providing fly stocks used in this study. This research was supported by a grant from the
677 National Institutes of Health to B.L. Goode (R35 GM134895). This work is also
678 supported by National Institutes of Health grants R01 GM105984 and R35 GM144115
679 to A.C. Martin.

680

681 **References**

682 Afshar, K., B. Stuart, and S.A. Wasserman. 2000. Functional analysis of the *Drosophila*
683 diaphanous FH protein in early embryonic development. *Development*.
684 127:1887-1897.

685 Algrain, M., O. Turunen, A. Vaheri, D. Louvard, and M. Arpin. 1993. Ezrin contains
686 cytoskeleton and membrane binding domains accounting for its proposed role as
687 a membrane-cytoskeletal linker. *Journal of Cell Biology*. 120:129-139.
688 Callaini, G., R. Dallai, and M.G. Riparbelli. 1992. Cytochalasin induces spindle fusion in
689 the syncytial blastoderm of the early *Drosophila* embryo. *Biology of the Cell*.
690 74:249-254.
691 Camuglia, J.M., A.R.A. Yeh, and A.C. Martin. 2021. Extracellular | Tension and Tissue
692 Morphogenesis. *In* Encyclopedia of Biological Chemistry III (Third Edition). J.
693 Jez, editor. Elsevier, Oxford. 317-325.
694 Cant, K., B.A. Knowles, M.S. Mooseker, and L. Cooley. 1994. *Drosophila* singed, a
695 fascin homolog, is required for actin bundle formation during oogenesis and
696 bristle extension. *Journal of Cell Biology*. 125:369-380.
697 Cao, J., R. Albertson, B. Riggs, C.M. Field, and W. Sullivan. 2008. Nuf, a Rab11
698 effector, maintains cytokinetic furrow integrity by promoting local actin
699 polymerization. *Journal of Cell Biology*. 182:301-313.
700 Chou, T.B., and N. Perrimon. 1992. Use of a yeast site-specific recombinase to produce
701 female germline chimeras in *Drosophila. Genetics*. 131:643-653.
702 Chugh, P., and E.K. Paluch. 2018. The actin cortex at a glance. *Journal of Cell Science*.
703 131:jcs186254.
704 Davidson, A.J., T.H. Millard, I.R. Evans, and W. Wood. 2019. Ena orchestrates
705 remodelling within the actin cytoskeleton to drive robust *Drosophila* macrophage
706 chemotaxis. *Journal of Cell Science*. 132:jcs224618.
707 Foe, V.E., C.M. Field, and G.M. Odell. 2000. Microtubules and mitotic cycle phase
708 modulate spatiotemporal distributions of F-actin and myosin II in *Drosophila*
709 syncytial blastoderm embryos. *Development*. 127:1767-1787.
710 Frangi, A.F., W.J. Niessen, K.L. Vincken, and M.A. Viergever. 1998. Multiscale vessel
711 enhancement filtering. Springer Berlin Heidelberg. 130-137.
712 Fukuda, M. 2002. The C2A domain of synaptotagmin-like protein 3 (Slp3) is an atypical
713 calcium-dependent phospholipid-binding machine: comparison with the C2A
714 domain of synaptotagmin I. *Biochem J*. 366:681-687.
715 Fukuda, M., T.S. Kuroda, and K. Mikoshiba. 2002. Slac2-a/Melanophilin, the Missing
716 Link between Rab27 and Myosin Va. *Journal of Biological Chemistry*. 277:12432-
717 12436.
718 Galvez-Santisteban, M., A.E. Rodriguez-Fraticelli, D.M. Bryant, S. Vergarajauregui, T.
719 Yasuda, I. Banon-Rodriguez, I. Bernascone, A. Datta, N. Spivak, K. Young, C.L.
720 Slim, P.R. Brakeman, M. Fukuda, K.E. Mostov, and F. Martin-Belmonte. 2012.
721 Synaptotagmin-like proteins control the formation of a single apical membrane
722 domain in epithelial cells. *Nat Cell Biol*. 14:838-849.
723 Gary, R., and A. Bretscher. 1995. Ezrin self-association involves binding of an N-
724 terminal domain to a normally masked C-terminal domain that includes the F-
725 actin binding site. *Molecular Biology of the Cell*. 6:1061-1075.
726 Gorfinkiel, N., and A.M. Arias. 2007. Requirements for adherens junction components in
727 the interaction between epithelial tissues during dorsal closure in *Drosophila*.
728 *Journal of Cell Science*. 120:3289-3298.

729 Gould, K.L., A. Bretscher, F.S. Esch, and T. Hunter. 1989. cDNA cloning and
730 sequencing of the protein-tyrosine kinase substrate, ezrin, reveals homology to
731 band 4.1. *The EMBO Journal*. 8:4133-4142.
732 Gratz, S.J., C.D. Rubinstein, M.M. Harrison, J. Wildonger, and K.M. O'Connor-Giles.
733 2015. CRISPR-Cas9 Genome Editing in *Drosophila*. *Current Protocols in*
734 *Molecular Biology*. 111.
735 Grevengoed, E.E., D.T. Fox, J. Gates, and M. Peifer. 2003. Balancing different types of
736 actin polymerization at distinct sites. *Journal of Cell Biology*. 163:1267-1279.
737 He, B., A. Martin, and E. Wieschaus. 2016. Flow-dependent myosin recruitment during
738 *Drosophila* cellularization requires zygotic dunk activity. *Development*. 143:2417-
739 2430.
740 Holly, R.M., L.M. Mavor, Z. Zuo, and J.T. Blankenship. 2015. A rapid, membrane-
741 dependent pathway directs furrow formation through RalA in the early *Drosophila*
742 embryo. *Development*. 142:2316-2328.
743 Jayanandanan, N., R. Mathew, and M. Leptin. 2014. Guidance of subcellular
744 tubulogenesis by actin under the control of a synaptotagmin-like protein and
745 Moesin. *Nature Communications*. 5.
746 Jiang, T., and T.J.C. Harris. 2019. Par-1 controls the composition and growth of cortical
747 actin caps during *Drosophila* embryo cleavage. *Journal of Cell Biology*.
748 218:4195-4214.
749 Jodoin, J.N., Coravos, J.S., Chanet, S., Vasquez, C.G., Tworoger, M., Kingston, E.R.,
750 Perkins, L.A., Perrimon, N., Martin, A.C. 2015. Stable Force Balance between
751 Epithelial Cells Arises from F-Actin Turnover. *Developmental Cell*. 35:685-697.
752 Koenderink, G.H., and E.K. Paluch. 2018. Architecture shapes contractility in
753 actomyosin networks. *Current Opinion in Cell Biology*. 50:79-85.
754 Krueger, D., T. Quinkler, S.A. Mortensen, C. Sachse, and S. De Renzis. 2019. Cross-
755 linker–mediated regulation of actin network organization controls tissue
756 morphogenesis. *Journal of Cell Biology*. 218:2743-2761.
757 Kuroda, T.S., H. Ariga, and M. Fukuda. 2003. The Actin-Binding Domain of Slac2-
758 a/Melanophilin Is Required for Melanosome Distribution in Melanocytes.
759 *Molecular and Cellular Biology*. 23:5245-5255.
760 Lecuit, T., R. Samanta, and E. Wieschaus. 2002. slam Encodes a Developmental
761 Regulator of Polarized Membrane Growth during Cleavage of the *Drosophila*
762 Embryo. *Developmental Cell*. 2:425-436.
763 Lecuit, T., and A.S. Yap. 2015. E-cadherin junctions as active mechanical integrators in
764 tissue dynamics. *Nature Cell Biology*. 17:533-539.
765 Lee, M.T., A.R. Bonneau, and A.J. Giraldez. 2014. Zygotic Genome Activation During
766 the Maternal-to-Zygotic Transition. *Annual Review of Cell and Developmental*
767 *Biology*. 30:581-613.
768 Lyakhova, T.A., and J.D. Knight. 2014. The C2 domains of granuphilin are high-affinity
769 sensors for plasma membrane lipids. *Chemistry and Physics of Lipids*. 182:29-
770 37.
771 Maître, J.-L., H. Berthoumieux, S.F.G. Krens, G. Salbreux, F. Jülicher, E. Paluch, and
772 C.-P. Heisenberg. 2012. Adhesion Functions in Cell Sorting by Mechanically
773 Coupling the Cortices of Adhering Cells. *Science*. 338:253-256.

774 Martin, A.C., M. Gelbart, R. Fernandez-Gonzalez, M. Kaschube, and E.F. Wieschaus.
775 2010. Integration of contractile forces during tissue invagination. *Journal of Cell*
776 *Biology*. 188:735-749.
777 McCartney, B.M., D.G. McEwen, E. Grevengoed, P. Maddox, A. Bejsovec, and M.
778 Peifer. 2001. *Drosophila* APC2 and Armadillo participate in tethering mitotic
779 spindles to cortical actin. *Nature Cell Biology*. 3:933-938.
780 Mizuno, K., T. Fujita, H. Gomi, and T. Izumi. 2016. Granuphilin exclusively mediates
781 functional granule docking to the plasma membrane. *Scientific Reports*. 6:23909.
782 Pilot, F., J.-M. Philippe, C.L. Lemmers, J.-P. Chauvin, and T. Lecuit. 2006a.
783 Developmental control of nuclear morphogenesis and anchoring by *charleston*,
784 identified in a functional genomic screen of *Drosophila* cellularisation.
785 *Development*. 133:711-723.
786 Pilot, F., J.M. Philippe, C. Lemmers, and T. Lecuit. 2006b. Spatial control of actin
787 organization at adherens junctions by a synaptotagmin-like protein Btsz. *Nature*.
788 442:580-584.
789 Plastino, J., and L. Blanchoin. 2019. Dynamic stability of the actin ecosystem. *Journal of*
790 *Cell Science*. 132:jcs219832.
791 Postner, M.A., and E.F. Wieschaus. 1994. The nullo protein is a component of the actin-
792 myosin network that mediates cellularization in *Drosophila* melanogaster
793 embryos. *Journal of Cell Science*. 107:1863-1873.
794 Riggs, B., W. Rothwell, S. Mische, G.R.X. Hickson, J. Matheson, T.S. Hays, G.W.
795 Gould, and W. Sullivan. 2003. Actin cytoskeleton remodeling during early
796 *Drosophila* furrow formation requires recycling endosomal components Nuclear-
797 fallout and Rab11. *Journal of Cell Biology*. 163:143-154.
798 Rikhy, R., M. Mavrakis, and J. Lippincott-Schwartz. 2015. Dynamin regulates
799 metaphase furrow formation and plasma membrane compartmentalization in the
800 syncytial *Drosophila* embryo. *Biology Open*. 4:301-311.
801 Roh-Johnson, M., G. Shemer, C.D. Higgins, J.H. McClellan, A.D. Werts, U.S. Tulu, L.
802 Gao, E. Betzig, D.P. Kiehart, and B. Goldstein. 2012. Triggering a Cell Shape
803 Change by Exploiting Preexisting Actomyosin Contractions. *Science*. 335:1232-
804 1235.
805 Rothwell, W.F., P. Fogarty, C.M. Field, and W. Sullivan. 1998. Nuclear-fallout, a
806 *Drosophila* protein that cycles from the cytoplasm to the centrosomes, regulates
807 cortical microfilament organization. *Development*. 125:1295-1303.
808 Schejter, E.D., and E. Wieschaus. 1993. bottleneck acts as a regulator of the
809 microfilament network governing cellularization of the *Drosophila* embryo. *Cell*.
810 75:373-385.
811 Serano, J., and G.M. Rubin. 2003. The *Drosophila* synaptotagmin-like protein bitesize is
812 required for growth and has mRNA localization sequences within its open
813 reading frame. *Proc Natl Acad Sci U S A*. 100:13368-13373.
814 Shekhar, S. 2017. Microfluidics-Assisted TIRF Imaging to Study Single Actin Filament
815 Dynamics. *Current Protocols in Cell Biology*. 77.
816 Sherlekar, A., G. Mundhe, P. Richa, B. Dey, S. Sharma, and R. Rikhy. 2020. F-BAR
817 domain protein Syndapin regulates actomyosin dynamics during apical cap
818 remodeling in syncytial *Drosophila* embryos. *J Cell Sci*. 133.

819 Simpson, L., and E. Wieschaus. 1990. Zygotic activity of the nullo locus is required to
820 stabilize the actin-myosin network during cellularization in *Drosophila*.
821 *Development*. 110:851-863.
822 Sokac, A.M., N. Biel, and S. De Renzis. 2023. Membrane-actin interactions in
823 morphogenesis: Lessons learned from *Drosophila* cellularization. *Seminars in*
824 *Cell & Developmental Biology*. 133:107-122.
825 Sokac, A.M., and E. Wieschaus. 2008. Local Actin-Dependent Endocytosis Is
826 Zygotically Controlled to Initiate *Drosophila* Cellularization. *Developmental Cell*.
827 14:775-786.
828 Spracklen, A.J., T.N. Fagan, K.E. Lovander, and T.L. Tootle. 2014. The pros and cons
829 of common actin labeling tools for visualizing actin dynamics during *Drosophila*
830 oogenesis. *Developmental Biology*. 393:209-226.
831 Spracklen, A.J., E.M. Thornton-Kolbe, A.N. Bonner, A. Florea, P.J. Compton, R.
832 Fernandez-Gonzalez, and M. Peifer. 2019. The Crk adapter protein is essential
833 for *Drosophila* embryogenesis, where it regulates multiple actin-dependent
834 morphogenic events. *Molecular Biology of the Cell*. 30:2399-2421.
835 Spudich, J.A., and S. Watt. 1971. The Regulation of Rabbit Skeletal Muscle
836 Contraction: I. BIOCHEMICAL STUDIES OF THE INTERACTION OF THE
837 TROPOMYOSIN-TROPONIN COMPLEX WITH ACTIN AND THE
838 PROTEOLYTIC FRAGMENTS OF MYOSIN. *Journal of Biological Chemistry*.
839 246:4866-4871.
840 Stevenson, V., A. Hudson, L. Cooley, and W.E. Theurkauf. 2002. Arp2/3-Dependent
841 Psuedocleavage Furrow Assembly in Syncytial *Drosophila* Embryos. *Current*
842 *Biology*. 12:705-711.
843 Stevenson, V.A., J. Kramer, J. Kuhn, and W.E. Theurkauf. 2001. Centrosomes and the
844 Scrambled protein coordinate microtubule-independent actin reorganization.
845 *Nature Cell Biology*. 3:68-75.
846 Sullivan, W., P. Fogarty, and W. Theurkauf. 1993. Mutations affecting the cytoskeletal
847 organization of syncytial *Drosophila* embryos. *Development*. 118:1245-1254.
848 Tilney, L.G., P.S. Connelly, K.A. Vranich, M.K. Shaw, and G.M. Guild. 2000. Regulation
849 of Actin Filament Cross-linking and Bundle Shape in *Drosophila* Bristles. *Journal*
850 *of Cell Biology*. 148:87-99.
851 Webb, R.L., M.-N. Zhou, and B.M. McCartney. 2009. A novel role for an APC2-
852 Diaphanous complex in regulating actin organization in *Drosophila*.
853 *Development*. 136:1283-1293.
854 Wenzl, C., S. Yan, P. Laupsien, and J. Großhans. 2010. Localization of RhoGEF2
855 during *Drosophila* cellularization is developmentally controlled by slam.
856 *Mechanisms of Development*. 127:371-384.
857 Xie, Y., R. Budhathoki, and J.T. Blankenship. 2021. Combinatorial deployment of F-
858 actin regulators to build complex 3D actin structures in vivo. *eLife*. 10.
859 Zallen, J.A., Y. Cohen, A.M. Hudson, L. Cooley, E. Wieschaus, and E.D. Schejter. 2002.
860 SCAR is a primary regulator of Arp2/3-dependent morphological events in
861 *Drosophila*. *Journal of Cell Biology*. 156:689-701.
862 Zaman, R., A. Lombardo, C. Sauvanet, R. Viswanatha, V. Awad, L.E.-R. Bonomo, D.
863 McDermitt, and A. Bretscher. 2021. Effector-mediated ERM activation locally

inhibits RhoA activity to shape the apical cell domain. *Journal of Cell Biology*. 220.

Zhang, Y., J.C. Yu, T. Jiang, R. Fernandez-Gonzalez, and T.J.C. Harris. 2018. Collision of Expanding Actin Caps with Actomyosin Borders for Cortical Bending and Mitotic Rounding in a Syncytium. *Developmental Cell*. 45:551-564.e554.

Zheng, L., L.A. Sepúlveda, R.C. Lua, O. Lichtarge, I. Golding, and A.M. Sokac. 2013. The Maternal-to-Zygotic Transition Targets Actin to Promote Robustness during Morphogenesis. *PLoS Genetics*. 9:e1003901.